Molecular distortions and the dynamics of spin crossover complexes

Shuang Yuan, Nadeem Natt, and Benjamin J. Powell*

School of Mathmatics and Physics, The University of Queensland, QLD 4072, Australia

E-mail: powell@physics.uq.edu.au

Abstract

We present a simple model of molecular distortions in spin crossover complexes, based on crystal field theory and transition state theory. This allows us to model the effect of molecular distortions on $T_{1/2}$, the characteristic temperature of thermal crossover and T_{LIESST}, the maximum temperature at which trapped excited high spin (HS) complexes are stable. We find that $T_{1/2}$ is a purely thermodynamic quantity as the kinetics are entirely determined by the relative free energies of the HS and low spin (LS) states ($\Delta G = G_{HS} - G_{LS}$). The average distortion across HS and LS species [$\overline{\Sigma} = (\Sigma_{HS} + \Sigma_{LS})/2$] has a significant impact on ΔG whereas the change in the metal-ligand bond length between HS and LS species ($\Delta d = d_{HS} - d_{LS}$), and the change in the molecular distortion between the HS and LS states ($\Delta\Sigma = \Sigma_{HS} - \Sigma_{LS}$) do not. Therefore, $\overline{\Sigma}$ has a large effect of $T_{1/2}$, whereas Δd and $\Delta\Sigma$ do not. T_{LIESST} is largely determined by the height of the barrier (E_b) between the metastable HS state and the LS state. E_b is strongly affected by Δd, $\Delta\Sigma$, and $\overline{\Sigma}$, so each of these quantities strongly impact T_{LIESST}. Thus, decreasing the average distortion across HS and LS species will increase T_{LIESST} and decrease $T_{1/2}$, which may provide a route to high temperature spin-state switching. Increasing the change in the metal-ligand bond length between

the HS and LS species or the molecular distortion between the HS and LS states will increase T_{LIESST} without substantially changing $T_{1/2}$.

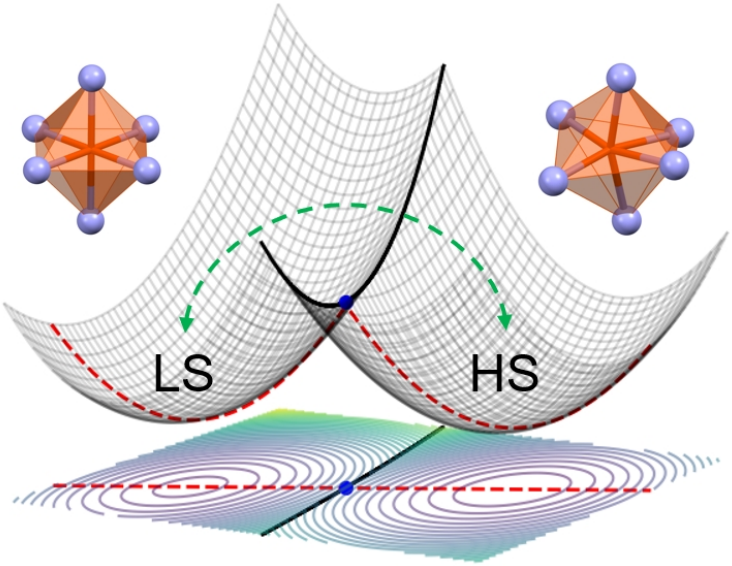

Graphical abstract.

Introduction

Numerous coordination compounds of first-row transition metal ions undergo a reversible change in electronic configuration between a low-spin (LS) state and a high-spin (HS) state, a process known as spin crossover (SCO).[1] The SCO phenomenon can be induced by various external stimuli, including temperature variations,[2] pressure,[3] magnetic[4] or electric fields,[5] and light irradiation.[6] The intrinsic small size and switchable spin states of SCO materials make them suitable for potential applications such as molecular switches,[7] nano-sensors,[8] and memory devices.[9]

The study of structure-property relationships plays a crucial role in manipulating stable and controllable SCO materials. In SCO molecules, the central metal ion is typically coordinated by six ligands, with the inner coordination sphere generally exhibiting approximately octahedral symmetry (O_h).[10] In an octahedral symmetric ligand field, the $3d$ orbitals of the

ion split into two sets: the higher-energy e_g orbitals and the lower-energy t_{2g} orbitals. In the most studied iron(II)-based SCO complexes, in the LS state, six electrons occupy the t_{2g} orbitals, whereas in the HS state, two electrons are promoted to the higher-energy e_g orbitals. A direct consequence of occupying the anti-bonding e_g orbitals is a significant increase in the metal-ligand bond length. For many iron(II) complexes with nitrogen-based ligands, the metal-ligand bond length increases (Δd) by $\sim 10\%$ when transitioning from the low-spin (LS) state to the high-spin (HS) state, resulting in an $\sim 25\%$ increase in the volume of the coordination octahedron.[11] The strength of the ligand field is highly dependent on the metal-ligand bond length,[10] which in turn dictates the energy gap between the e_g and t_{2g} orbitals.[12] This energy gap significantly influences both the relaxation time in light-induced excited spin-state trapping (LIESST) experiments and, $T_{1/2}$, the characteristic temperature of thermally-induced SCO.[13] As a result, many theoretical studies make a single-mode approximation where the metal-ligand bond length is the only vibrational mode considered explicitly.[14–27] These simulations effectively reproduce many experimental observations, including the inverse relationship[28] between the highest temperature at which the trapped state remains stable following LIESST (T_{LIESST}) and the characteristic temperature of the thermal transition ($T_{1/2}$), the hysteresis observed in thermally-induced SCO, and structure-property relationships for multistep transitions.[22]

However, the single-mode approximation of SCO molecules encounters challenges in explaining certain experimental observations. Chastanet *et al.*[28] noted that an increase in Δd generally correlates with a larger potential barrier for the HS$\rightarrow$LS transition, leading to a higher T_{LIESST}. Nevertheless, studies show that complexes made of phosphorus-based ligands, despite having larger Δd, do not exhibit a significant improvement in T_{LIESST} compared to nitrogen-based ligands, that have smaller Δd.[29] This discrepancy suggests that a comprehensive understanding of SCO behavior requires consideration of additional structural changes beyond just metal-ligand bond length.

A key structural change between the LS and HS states, which has been widely observed

in experiments,[30–33] is the distortion of the inner coordination sphere. Few, if any, SCO complexes exhibit perfect octahedral symmetry. Furthermore, complexes are typically more symmetrical in the LS state than the HS state. For example, $[Fe(bpp)_2]^{2+}$ derivatives show D_{2d} symmetry in the LS state but deviate from this symmetry in the HS state.[34] A similar process is also observed in many other iron(II) complexes,[35–38] as well as many cobalt(II),[39–42] manganese(II),[43–48] zinc(II),[49–52] and iron(III)[53–55] SCO complexes.

The molecular distortion from the octahedral symmetry can be defined in several ways. Commonly used parameters include the angular (Σ) and torsional (Θ) distortions.[56] Σ gives a general description of the departure of the inner coordination sphere from octahedral symmetry, whereas Θ represents a distortion from the octahedral symmetry to the trigonal prismatic symmetry.

Molecular distortion has been shown to significantly influence both thermally-induced SCO and LIESST. Marchivie and co-workers[57] reviewed several experimental observations of $[FeL_n(NCS)_2]$ complexes and discovered a linear relationship between T_{LIESST} and the torsional distortion difference between the high-spin (HS) and low-spin (LS) states ($\Delta\Theta = \Theta_{HS} - \Theta_{LS}$). Additionally, they found a inverse relationship between $T_{1/2}$ and $\Delta\Theta$, indicating the crucial role of distortion in SCO.

Boilleau and colleagues[58] investigated these experimental observations with using density functional theory. They calculated the harmonic potential energy surfaces for the LS and HS states as functions of the average metal-ligand bond length and torsional distortion differences. Their results show that the potential barrier, which correlates strongly with T_{LIESST}, has a linear relationship with torsional distortion, while the minimum energy difference between the LS and HS states, assumed to determine $T_{1/2}$, exhibits a inverse relationship with torsional distortion.

In this paper, we present a minimal model based on crystal field theory (CFT) to account for molecular distortions in SCO molecules.[59] We introduce both symmetric and asymmetric vibrational modes in our model, resulting in a C_{4v} symmetric ligand field. Under the C_{4v}

symmetric ligand field, both the single-electron orbitals and the d^6 electronic configuration, originally associated with the O_h symmetric ligand field, split into additional energy terms. Based on these split energy terms, we construct a 2D double-well potential surface as a function of the two vibrational modes, effectively describing the transition between the LS and HS states. Using transition state theory (TST),[60] we simulate thermally-induced SCO as well as the relaxation of the kinetically trapped HS state which is obtained after LIESST process. We find clear relationships of the SCO properties with the average angular distortion ($\overline{\Sigma} = (\Sigma_{HS} + \Sigma_{LS})/2$) and the angular distortion difference ($\Delta\Sigma = \Sigma_{HS} - \Sigma_{LS}$) between the HS and LS molecular geometries. Larger $\overline{\Sigma}$ leads to a significant increase in $T_{1/2}$ and a slightly decrease in T_{LIESST}. Whereas, increasing $\Delta\Sigma$ does not change $T_{1/2}$ but significantly increases T_{LIESST}.

Model

Geometric changes due to spin crossover

The structural changes that accompany a spin-state transition in an octahedral transition metal complex are conventionally parameterized[56] by the average metal-ligand bond length,

$$d = \frac{1}{6}\sum_{i=1}^{6} d_i, \tag{1}$$

where d_i is the ith metal-ligand bond length; and the angular distortion,

$$\Sigma = \sum_{i=1}^{12} \left|90^\circ - \phi_i\right|, \tag{2}$$

where ϕ_i is the angle subtended by a pair of ligands from the metal, as shown in figure 1(a).

We build our model from CFT,[59] as this is the simplest theory that captures SCO and we aim, here, to understand the impact of molecular distortions on SCO at a general level. Thus,

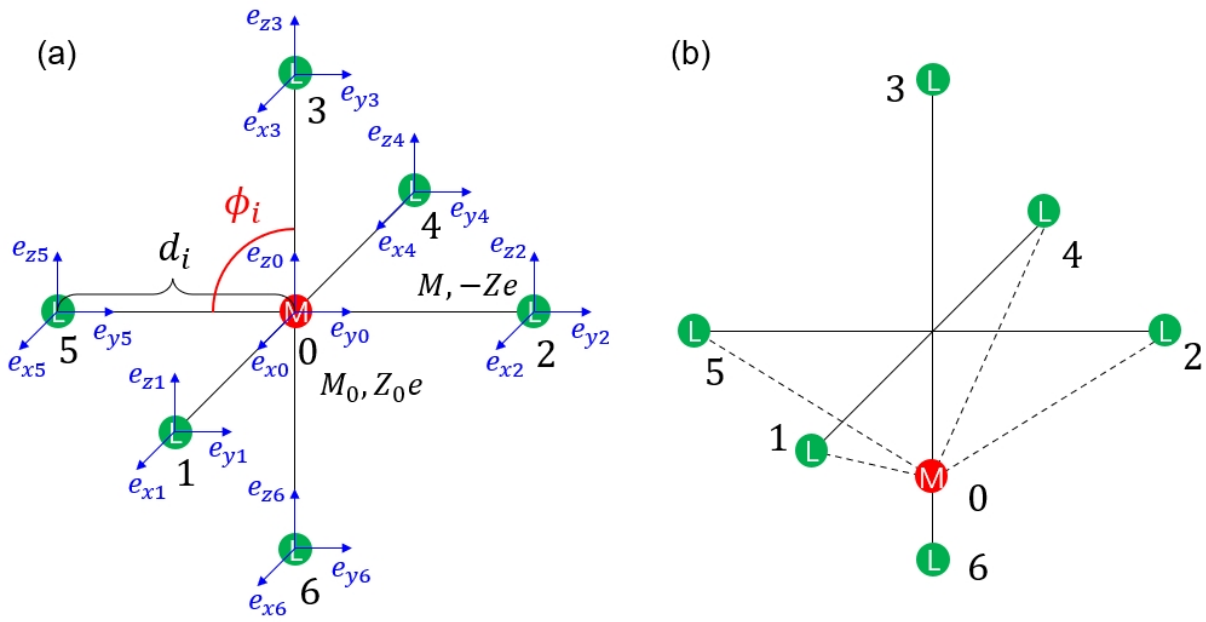

Figure 1: Positions of metal and ligands in a single SCO molecule. In crystal field theory one assumes that the metal (red) with mass M_0 and charge Z_0e is surrounded by six ligands (green) with mass M and charge $-Ze$. (a) An SCO molecule with perfect octahedral (O_h) symmetry. The distance between each ligand and metal is d_i. The vectors $\hat{\boldsymbol{e}}_{xi}$, $\hat{\boldsymbol{e}}_{yi}$ and $\hat{\boldsymbol{e}}_{zi}$, with $i = 0$ for the metal and $i = 1 - 6$ for the ligands, form an orthogonal coordinate system fixed at the equilibrium positions of the atoms. (b) Distortion along the $T_{1u}^{(\mathrm{II})}$ mode reduces the symmetry of the molecule to C_{4v}.

we treat an octahedral SCO complex as a hydrogen-like metal atom with charge $Z_0 e$ and mass M_0 surrounded by six ligands represented by point charges with charge $-Ze$ and mass M, figure 1(a). This model has 15 vibrational modes. In order to construct a simple model we will treat only two of these explicitly, and average over remaining 13 modes. We will show below that it is reasonable to expect that a two-mode model captures the main features of a 15 model – as has been argued previously in very different contexts.[61] It has been shown previously,[14–27] that the A_{1g} breathing mode, which only describes changes in the average metal-ligand bond length is crucial for understanding the dynamics of SCO. However, this mode does not break the octahedral (O_h) symmetry of the complex. Therefore, at least one more mode needs to be included to describe the angular distortion of the complex. Which mode we include is somewhat arbitrary as there is no clear pattern among octahedral SCO complexes as to which mode undergoes the second largest distortion after the A_{1g} breathing mode. Here we choose to include the T_{1u} mode, sketched in figure 1(b). The geometry of a complex can thus be written as

$$\boldsymbol{Q} = Q_A \hat{\boldsymbol{e}}_A + Q_T \hat{\boldsymbol{e}}_T, \tag{3}$$

where $\boldsymbol{Q}$ is the 15-dimensional vector describing the geometry of the complex, Q_A and Q_T are the magnitudes of A_{1g} and T_{1u} modes,

$$\hat{\boldsymbol{e}}_A = \frac{1}{\sqrt{6}} \left(\hat{\boldsymbol{e}}_{1x} + \hat{\boldsymbol{e}}_{2y} + \hat{\boldsymbol{e}}_{3z} - \hat{\boldsymbol{e}}_{4x} - \hat{\boldsymbol{e}}_{5y} - \hat{\boldsymbol{e}}_{6z} \right), \tag{4a}$$

$$\hat{\boldsymbol{e}}_T = \sqrt{\frac{2M}{2M + M_0}} \hat{\boldsymbol{e}}_{0z} - \sqrt{\frac{M_0}{2\left(2M + M_0\right)}} \left(\hat{\boldsymbol{e}}_{3z} - \hat{\boldsymbol{e}}_{6z} \right). \tag{4b}$$

are the basis vectors of A_{1g} and T_{1u} modes, and the Cartesian basis vectors, $\hat{\boldsymbol{e}}_{in}$, are marked in figure 1(a).

The relationship between $\{Q_A, Q_T\}$ and $\{d, \Sigma\}$ is explored in figure 2. As one might expect, the average metal-ligand bond length (d) is mainly determined by Q_A, but Q_T also

has a weak influence on d. Likewise, the degree of angular distortion (Σ) of the system is mainly determined by Q_T but, given $Q_T \neq 0$, Q_A also has a weak influence on Σ.

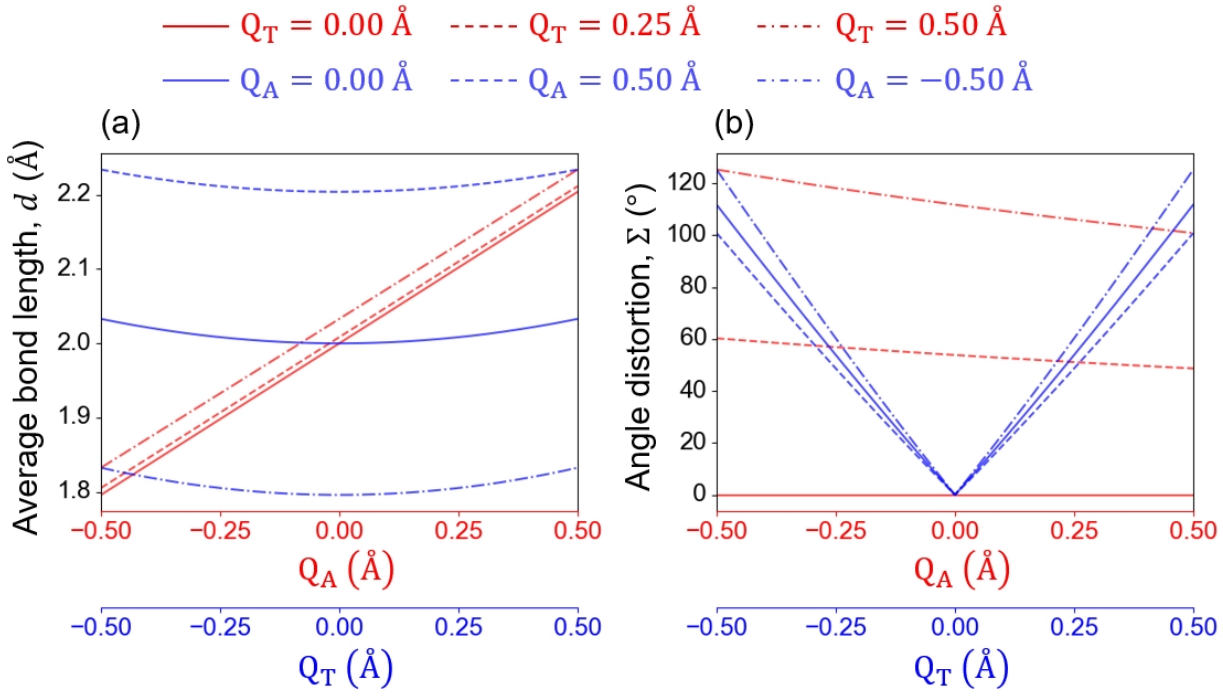

Figure 2: Variation of (a) the average metal-ligand bond length, d, and (b) the angular distortion, Σ, of the system with the coordinates Q_A (red lines) and Q_T (blue lines). The average metal-ligand bond length for $Q_A = 0$ Å and $Q_T = 0$ Å is set to $d_0 = 2$ Å.

Crystal field theory

For $Q_T \neq 0$ the symmetry of the complex is lowered from O_h to C_{4v}. It is well known[62] that this lifts the orbital degeneracy, as sketched in figure 3. The change in the orbital energy eigenvalues as d and Σ (or equivalently Q_A and Q_T) vary can readily be calculated, figure 4 (see Supplementary Information for details of the calculation). Two important trends are found. Firstly, as d increases, the crystal field becomes weaker, thus the splitting between the e_g and t_{2g} states decreases. Secondly, the crystal field splitting within the e_g and t_{2g} manifolds increases as Σ increases.

Based on the orbital energies, we calculate the six-electron (d^6) energy terms including electron-electron interactions (as detailed in the Supplementary Information). To do this we

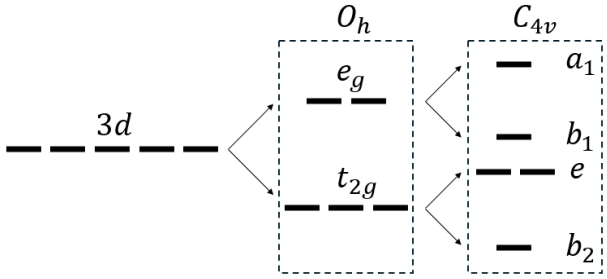

Figure 3: Splitting of the single $3d$-electron of the metal atom in O_h and C_{4v} symmetric ligand field.

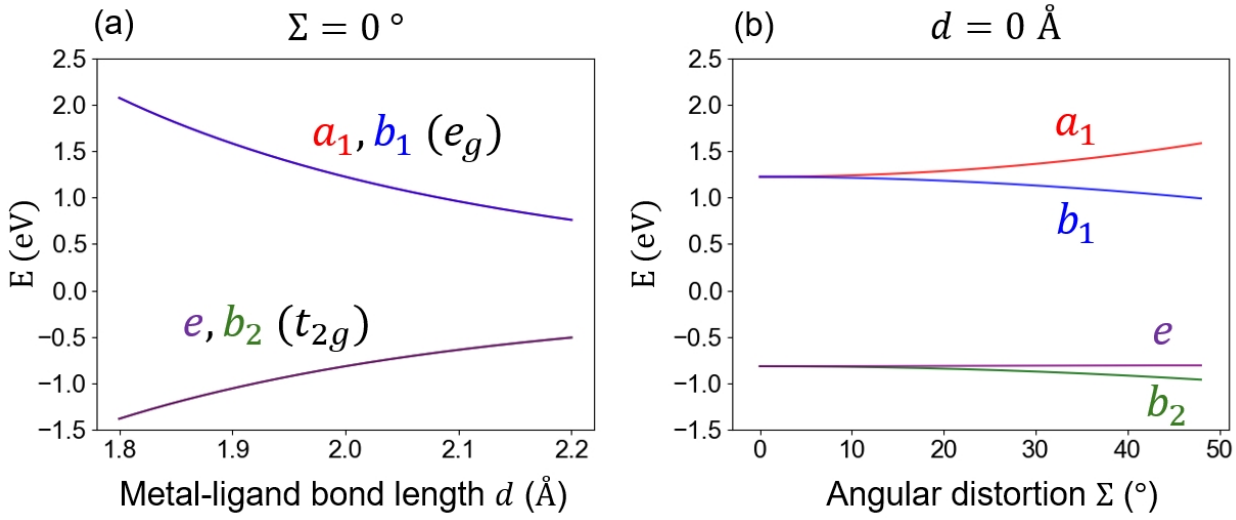

Figure 4: Single electron (d^1) orbital energies from crystal field theory. (a) Variation in orbital energies with the metal-ligand bond length (d), for an octahedrally symmetric molecule ($\Sigma = 0°$). The energy splitting between e_g and t_{2g} states decreases as d increases. (b) Changes in orbital energies with the angular distortion (Σ). The energy splitting within the e_g and t_{2g} manifolds increases with the angular distortion. All other parameters are set to the default values given in Table 1.

use the Racah parameterization of the electron-electron Coulomb interactions and make the standard assumption that the ratio of Racah parameters is fixed, $C/B = 4.81$.[59] Thus the electron-electron interaction strength is determined by B. We include only the five lowest energy terms in our model, namely, the low-spin [LS; $^1A_1$ ($^1A_1$)], intermediate spin [IS; $^3T_1$ (^3E, $^3A_2$)], and high-spin [HS; $^5T_2$ (^5E, $^5B_2$)] states, where the symmetry labels are given for O_h (C_{4v}) symmetry, relevant for $Q_T = 0$ ($Q_T \neq 0$) respectively. The dependence of the energies of the d^6 terms on the geometry of the complex are explored in figure 5. We see that changes in bond length have the largest influence on the relative stability of the HS and LS states, and that angular distortions partially lift the orbital degeneracy of the HS states.

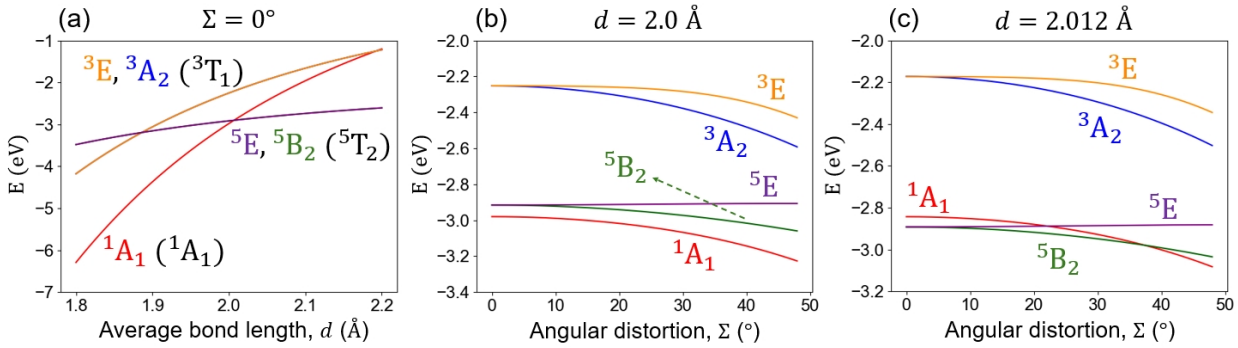

Figure 5: The lowest energy terms of the LS ($^1A_1$), IS ($^3A_2$, ^3E) and HS (^5E, $^5B_2$) states calculated from the crystal field theory of a d^6 SCO metal center in an C_{4v} symmetry ligand field. (a) Variation of energies with metal-ligand bond length (d). (b,c) Variation of energies with angular distortion (Σ), this splits the ^3E term from the $^3A_2$ term and the ^5E term from the $^5B_2$ term. All parameters are taken as the default values, given in table 1, except (a) $\Sigma = 0°$, (b) $d = 2.0$ Å, and (c) $d = 2.012$ Å.

Spin-orbit coupling

Transition between the LS, IS, and HS states are spin-forbidden. Thus they can only be mediated by spin-orbit coupling.[10,17,63] Spin-orbit coupling also causes zero-field splitting of the IS and HS states, see figure 6 and section S2.4. The most important effect, for what follows, is that the ^3E and ^5E states are both split into three different manifolds of degenerate terms.

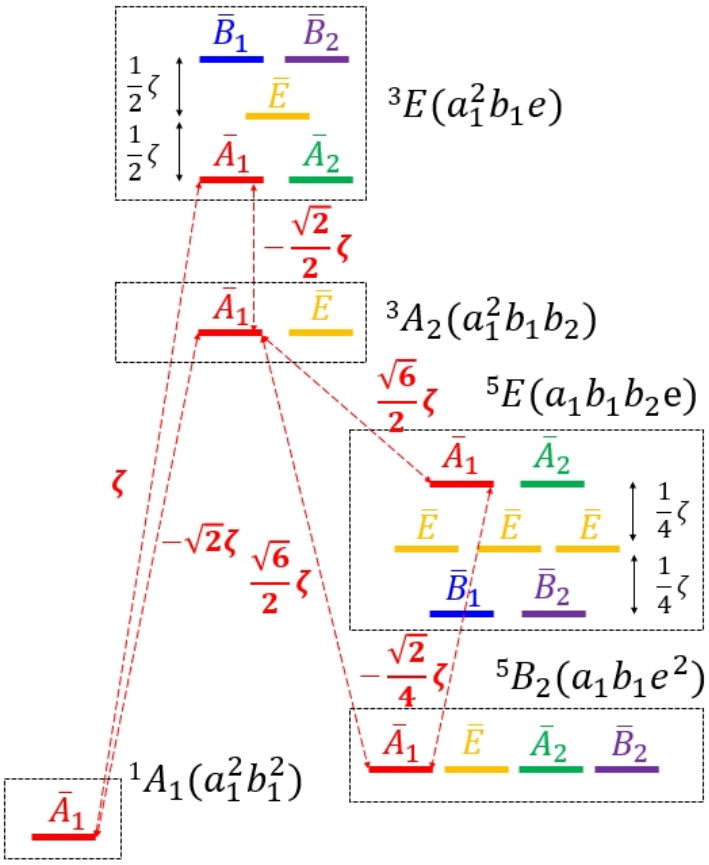

Figure 6: Key spin-orbit interactions for SCO in a d^6 complex with a C_{4v} symmetric ligand field. For simplicity, only the spin-orbit coupling between $\overline{A}_1$ states are shown and we include only the LS ($^1A_1$), IS (^3E, $^3A_2$) and HS (^5E, $^5B_2$) states. The superscripts label the spin multiplicity $(2S+1)$ of the term, where S is the total spin quantum number. A_1, B_2 and E are the irreducible representations of C_{4v} group, which have orbital degeneracies of 1, 1 and 2 respectively. $\overline{A}_1$, $\overline{A}_2$, $\overline{B}_2$ and $\overline{E}$ label the irreducible representations of the double group, and have *total* degeneracies of 1, 1, 1 and 2 respectively. The arrows indicate the spin-orbit coupling between states, and ζ represents the spin-orbit coupling strength.

The usual (single) group theoretic labels are no longer strictly relevant once spin-orbit coupling is included, therefore we henceforth label the terms by the double group representations of C_{4v}, figure 6. Henceforth, we will distinguish the double group representations by placing a line above the relevant symbol; i.e., $\overline{A}_1$ is a representation of the double group whereas A_1 a representation of the single group.

Spin-orbit coupling is only non-zero between terms that have the same double-group representation. One immediately sees that only $\overline{A}_1$ terms appear in all of the LS, IS, and HS states. Therefore, these terms play a crucial role in spin crossover.

Diabatic low-energy model

We assume that the A_{1g} and T_{1u} modes explicitly included in our model are classical and harmonic. Thus the diabatic potential energy surfaces are

$$\begin{aligned} V_{\alpha,\overline{\psi}(\chi)}(Q_A, Q_T) = E_{\alpha,\overline{\psi}(\chi)}\left(d_0, Q_T^{(0)}\right) + \frac{1}{2}k_{\alpha A}\left(Q_A - \delta_{\alpha A}\right)^2 \\ + \frac{1}{2}k_{\alpha T}\left(Q_T - Q_T^{(0)} - \delta_{\alpha T}\right)^2, \end{aligned} \tag{5}$$

where $E_{\alpha,\overline{\psi}(\chi)}\left(d_0, Q_T^{(0)}\right)$ is the energy of the $\overline{\psi}(\chi)$th term of the αth spin state calculated from crystal field theory with the average metal-ligand bond length set to $d = d_0$ and the T_{1u} mode at $Q_T = Q_T^{(0)}$; here $\alpha \in \{\text{LS, IS, HS}\}$, $\overline{\psi}$ is a representations of the double group C_{4v} and χ is the parent representation of the single group C_{4v} (which is necessary to distinguish terms when more than one belong to the representation $\overline{\psi}$), $k_{\alpha A}$ and $k_{\alpha T}$ are spring constants for A_{1g} and T_{1u} modes respectively, $\delta_{\alpha A}$ and $\delta_{\alpha T}$ account for the difference in the minima of the vibrational modes in different spin states. For simplicity we set

$$\delta_{\alpha A} = \begin{cases} -\delta_A, & \alpha = \text{LS} \\ 0, & \alpha = \text{IS} \\ \delta_A, & \alpha = \text{HS} \end{cases}, \qquad \delta_{\alpha T} = \begin{cases} -\delta_T, & \alpha = \text{LS} \\ 0, & \alpha = \text{IS} \\ \delta_T, & \alpha = \text{HS} \end{cases}; \tag{6}$$

with this choice d_0 and $Q_T^{(0)}$ can be interpreted as either (a) the average bond length and the minimum energy value of the T_{1u} mode in the IS state, or (b) as the average of these quantities in the LS and HS states.

We assume all ligands are identical and are connected to the metal by identical springs. To model the changes of the metal-ligand bonds when the spin-state changes we set their spring constants to be

$$k_\alpha = \begin{cases} k - \kappa, & \alpha = \text{LS} \\ k, & \alpha = \text{IS} \\ k + \kappa, & \alpha = \text{HS} \end{cases} \tag{7}$$

where k is the spring constant of the metal ligand bonds in the IS state and κ is the softening (hardening) of the metal-ligand bonds in the HS (resp. LS) state. The effective masses, M_A and M_T, and effective spring constants in the αth spin-state, $k_{\alpha A}$ and $k_{\alpha T}$, for the A_1 and T_{1u} modes, respectively, are then

$$M_A = M, \tag{8a}$$

$$M_T = \frac{2MM_0}{M+M_0} \cdot \left(\sqrt{\frac{M_0}{2(2M+M_0)}} + \sqrt{\frac{2M}{2M+M_0}} \right)^2, \tag{8b}$$

$$k_{\alpha A} = k_\alpha, \tag{8c}$$

$$k_{\alpha T} = \frac{(2\sqrt{M} + \sqrt{M_0})^2}{2M+M_0} k_\alpha. \tag{8d}$$

As the frequencies, $\omega_{\alpha A}$ and $\omega_{\alpha T}$, of the A_1 and T_{1u} modes in spin state α are given by

$$\omega_{\alpha\nu} = \sqrt{\frac{k_{\alpha\nu}}{M_\nu}}, \tag{9}$$

where $\nu \in \{A, T\}$, we find that

$$\frac{\omega_{\alpha T}}{\omega_{\alpha A}} = \sqrt{1 + \frac{M}{M_0}}. \tag{10}$$

We plot the potential surfaces of the $\overline{A}_1$ symmetry LS, IS, and HS states along the path

$$\{Q_A, Q_T\} = \left\{ \ell, \frac{\delta_T}{\delta_A} \left(\ell - Q_A^{(0)} \right) + Q_T^{(0)} \right\}, \tag{11}$$

which passes through the minima of LS and HS states, in figure 7(a); we also mark the inter-term spin-orbit coupling coefficients in this plot. Explicitly, the Hamiltonian for the $\overline{A}_1$ states is

$$\hat{H} = \begin{pmatrix} V_{LS,\overline{A}_1(^1A_1)} & -\sqrt{2}\zeta & \zeta & 0 & 0 \\ -\sqrt{2}\zeta & V_{IS,\overline{A}_1(^3A_2)} & -\frac{1}{\sqrt{2}}\zeta & 0 & \frac{\sqrt{6}}{2}\zeta \\ \zeta & -\frac{1}{\sqrt{2}}\zeta & V_{IS,\overline{A}_1(^3E)} & \frac{\sqrt{6}}{2}\zeta & 0 \\ 0 & 0 & \frac{\sqrt{6}}{2}\zeta & V_{HS,\overline{A}_1(^5B_2)} & -\frac{\sqrt{2}}{4}\zeta \\ 0 & \frac{\sqrt{6}}{2}\zeta & 0 & -\frac{\sqrt{2}}{4}\zeta & V_{HS,\overline{A}_1(^5E)} \end{pmatrix}, \tag{12}$$

This model contains the key physics for SCO in a basis of diabatic states.

Adiabatic effective low-energy model

However, it is simpler to model SCO in terms of adiabatic states.[17] For electrons in 3*d*-orbitals the strength of the spin-orbit interaction, ζ, is about an order of magnitude smaller than that of the Coulomb interaction.[59] Therefore, to construct an effective low-energy model in an adiabatic basis we begin by integrating out the IS states via a canonical transformation,[17,64–66]

$$\hat{H}_{\text{eff}} = \sum_{\mu \in L} \hat{P}_\mu \hat{H} \hat{P}_\mu - \frac{1}{2} \sum_{\mu,\mu' \in \mathcal{L}} \sum_{\nu \in \overline{\mathcal{L}}} \left(\frac{\hat{P}_\mu \hat{H} \hat{P}_\nu \hat{H} \hat{P}_{\mu'}}{\left\langle \hat{P}_\nu \hat{H} \hat{P}_\nu \right\rangle - \left\langle \hat{P}_{\mu'} \hat{H} \hat{P}_{\mu'} \right\rangle} + \frac{\hat{P}_\mu \hat{H} \hat{P}_\nu \hat{H} \hat{P}_{\mu'}}{\left\langle \hat{P}_\nu \hat{H} \hat{P}_\nu \right\rangle - \left\langle \hat{P}_\mu \hat{H} \hat{P}_\mu \right\rangle} \right), \tag{13}$$

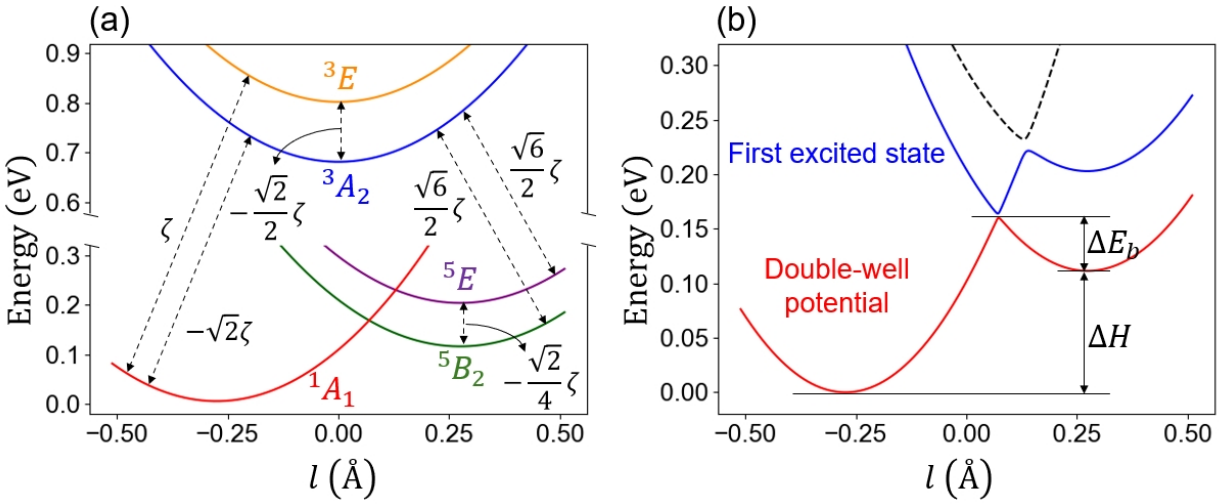

Figure 7: Potential surfaces of the $\overline{A}_1$ states along the path defined by equation 11, which passes through the minima of both the HS and LS states, for (a) diabatic and (b) adiabatic states. (a) Labels of potential energy surfaces indicate the symmetries of the parent states before including spin-orbit coupling. The dashed arrows indicate the spin-orbit coupling between different states. (b) The potential surfaces after integrating out the high-energy IS states. The lowest energy surface is the double-well potential. The first-excited state is not relevant to SCO, as the left minimum is a quantum superposition of the HS and LS states (with a small IS admixture) and right minimum is a HS state (cf. figure S1). The highest energy state (black dashed line) is a pure HS state. ΔE_b is the potential barrier for moving from the HS to the LS state, and ΔH is the enthalpy difference between two local minimums of the double-well potential. In both plots, parameters are set to the default values given in Table 1.

where $\hat{P}_\mu$ is a projector onto the μth subspace, the low-energy subspace, $\mathcal{L}$, contains the LS and HS states, and the high-energy subspace, $\overline{\mathcal{L}}$, contains the IS states. This amounts to treating the inter-term spin-orbit coupling at second order in perturbation theory.

After applying the canonical transformation the effective Hamiltonian, written in a basis of dressed low-energy states, is

$$\hat{H}_{\text{eff}} = \begin{pmatrix} \widetilde{V}_{^1A_1} & \lambda_1 & \lambda_2 \\ \lambda_1 & \widetilde{V}_{^5B_2} & -\frac{\sqrt{2}}{4}\zeta \\ \lambda_2 & -\frac{\sqrt{2}}{4}\zeta & \widetilde{V}_{^5E} \end{pmatrix}, \tag{14}$$

where

$$\widetilde{V}_{^1A_1}(\boldsymbol{Q}) = V_{LS,\overline{A}_1(^1A_1)} - \frac{\zeta^2}{2} \cdot \left(\frac{4}{V_{IS,\overline{A}_1(^3A_2)} - V_{LS,\overline{A}_1(^1A_1)}} + \frac{2}{V_{IS,\overline{A}_1(^3E)} - V_{LS,\overline{A}_1(^1A_1)}} \right), \tag{15a}$$

$$\widetilde{V}_{^5B_2}(\boldsymbol{Q}) = V_{HS,\overline{A}_1(^5B_2)} - \frac{\zeta^2}{2} \cdot \frac{3}{V_{IS,\overline{A}_1(^3E)} - V_{HS,\overline{A}_1(^5B_2)}}, \tag{15b}$$

$$\widetilde{V}_{^5E}(\boldsymbol{Q}) = V_{HS,\overline{A}_1(^5B_2)} - \frac{\zeta^2}{2} \cdot \frac{3}{V_{IS,\overline{A}_1(^3E)} - V_{HS,\overline{A}_1(^5E)}}, \tag{15c}$$

$$\lambda_1(\boldsymbol{Q}) = -\frac{\zeta^2}{2} \cdot \left(\frac{\sqrt{6}/2}{V_{IS,\overline{A}_1(^3E)} - V_{LS,\overline{A}_1(^1A_1)}} + \frac{\sqrt{6}/2}{V_{IS,\overline{A}_1(^3E)} - V_{HS,\overline{A}_1(^5B_2)}} \right), \tag{15d}$$

$$\lambda_2(\boldsymbol{Q}) = -\frac{\zeta^2}{2} \cdot \left(\frac{-\sqrt{3}}{V_{IS,\overline{A}_1(^3A_2)} - V_{LS,\overline{A}_1(^1A_1)}} + \frac{-\sqrt{3}}{V_{IS,\overline{A}_1(^3A_2)} - V_{HS,\overline{A}_1(^5E)}} \right). \tag{15e}$$

The effective low-energy Hamiltonian (equation 14) after the canonical transformation directly describes the connection between the dressed LS and HS states. Diagonalizing this matrix results an adiabatic basis consisting of a ground state double-well (DW) potential energy surface and two excited states, figure 7(b).

Mapping the double-well potential as a function of Q_A and Q_T, figure 8, reveals that the LS and HS states are separated by the seam, $\mathcal{S}$. The minimum of the seam is the saddle point between the two local minima. We define ΔE_b as the energy difference between the

saddle point and the HS local minimum, and ΔH as the potential difference between the local minima for LS and HS states, figure 7b. When the angular distortion of the system increases, ΔH increases but ΔE_b decreases, figure 9.

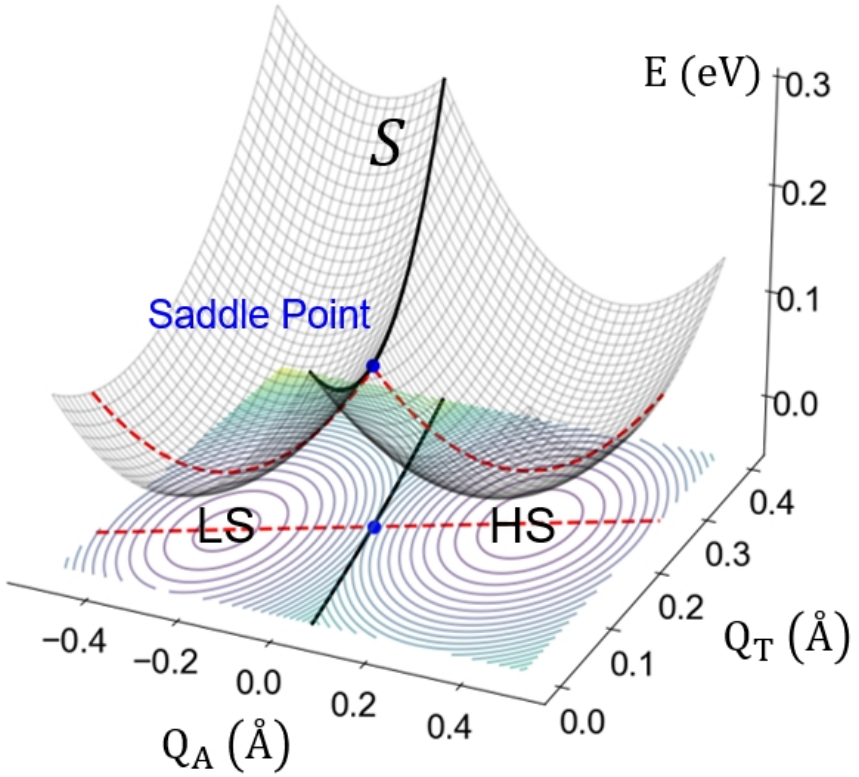

Figure 8: The DW potential as a function of Q_A and Q_T (all parameters are set to the default values given in Table 1). The black curve is the seam, $\mathcal{S}$, separating the LS (left) and HS (right) areas. The minimum of this curve is the saddle point. The red dashed line, defined in Eq. 11, connects the local minimums of the LS and HS areas, and passes close to the saddle point.

The first excited state also has two local minima in figures 7(b), S1. However, the state at local minimum at large ℓ (i.e., on the right hand side of figure 7(b)) has predominately ^5E HS character; and the state at small ℓ is a quantum superposition of the $^5B_2$ HS and $^1A_1$ LS states due to the avoided crossing of these states. Thus, the first excited state is of little importance for the equilibrium properties of SCO. Therefore, we neglect the two excited states and build a semi-classical model by considering the DW potential alone.

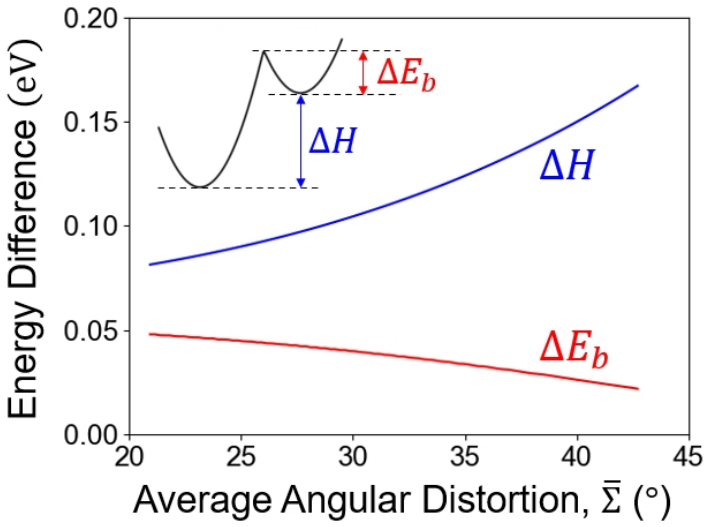

Figure 9: Variation of the minimum potential barrier (ΔE_b) and enthalpy difference (ΔH) of 2D double-well potential with the angular distortion $\overline{\Sigma}$. The plot uses the default parameters given in Table 1. Increasing $\overline{\Sigma}$ decreases ΔE_b, and increases ΔH.

Entropy and free energy of spin crossover

The A_{1g} and T_{1u} modes are explicitly included in the model. However, even if the the remaining thirteen vibration modes do not qualitatively change the crystal field theory they cannot be ignored as they contribute significantly to the entropy difference between LS and HS states, ΔS. For simplicity, we replace the thirteen different frequencies of these modes by a single 'average' frequency which we assume to be different in the for LS (ω_{LS}) and HS (ω_{HS}) states.[67]

Furthermore, one of the HS states has been subsumed into the DW potential, but the entropy of the remaining fourteen pure HS states also contributes to the entropy change on SCO. Treating the fourteen pure HS states at this level of approximation is equivalent to assuming that the transitions between different HS states occur much more rapidly that transitions from the LS to HS states.

Thus the entropy difference between the HS and LS states is

$$\Delta S(T) = 13\left(\frac{\hbar\omega_{\mathrm{HS}}}{T}\frac{1}{e^{\frac{\hbar\omega_{\mathrm{HS}}}{k_B T}}-1} - \frac{\hbar\omega_{\mathrm{LS}}}{T}\frac{1}{e^{\frac{\hbar\omega_{\mathrm{LS}}}{k_B T}}-1} + k_{\mathrm{B}}\ln\left[\frac{1-e^{\frac{\hbar\omega_{\mathrm{LS}}}{k_B T}}}{1-e^{\frac{\hbar\omega_{\mathrm{HS}}}{k_B T}}}\right]\right) + k_{\mathrm{B}}\ln\left[\frac{g_{HS}}{g_{LS}}\right], \quad (16)$$

where $g_{HS}/g_{LS} = 15$ is the ratio of the electronic degeneracies of the HS and LS states, $\hbar$ is the reduced Plank constant, T is the temperature, and k_{B} is Boltzmann's constant. With the implicit vibrational and electronic terms of the entropy included, the free energy is given by the lowest eigenvalue of

$$\hat{F} = \begin{pmatrix} \widetilde{V}_{^1A_1} & \lambda_1 & \lambda_2 \\ \lambda_1 & \widetilde{V}_{^5B_2} - T\Delta S(T) & -\frac{\sqrt{2}}{4}\zeta \\ \lambda_2 & -\frac{\sqrt{2}}{4}\zeta & \widetilde{V}_{^5E} - T\Delta S(T) \end{pmatrix}. \tag{17}$$

The entropy of the implicit degrees of freedom is largely responsible for driving the thermodynamic equilibrium from LS to HS as temperature increases, figure 10.

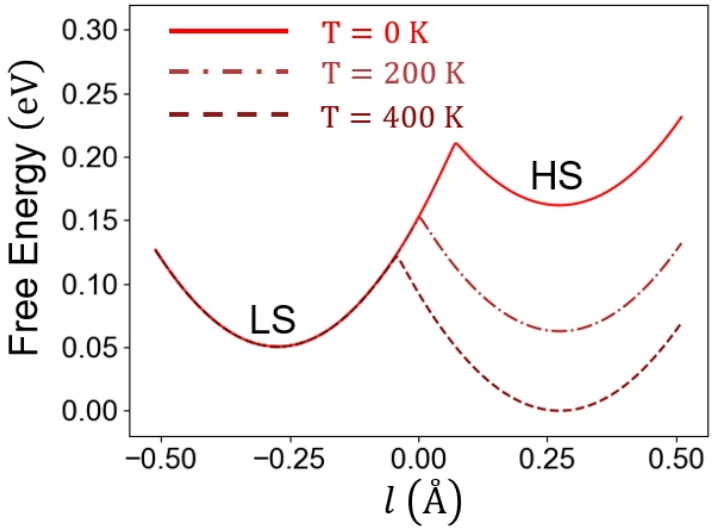

Figure 10: The double-well potential after including the entropy difference from the thirteen implicit vibration modes and fourteen pure HS states at different temperatures ($T = 0,\ 200,\ 400$ K). All other parameters are the default values given in Table 1. For $T > T_{1/2} \simeq 210$ K the local minimum of the HS state is the global minimum, whereas $T < T_{1/2}$ the local minimum of the LS state is the global minimum. This drives the spin crossover.

Parameterization of the model

We estimate the parameters from experiment. Typical ranges are given in table 1, along with 'default values' that we will use for most of our calculations. For those parameters that appear in the single mode model, we use the estimates given in our previous work.[17] We briefly justify the other parameter choices in the remainder of this section.

Table 1: Typical ranges of the parameters that appear in our model and the default values used in this paper

Parameter	Range	Default Value
M/M_0	≥ 1.5 [12,68]	2
Z_0/Z	5.167-5.212 [17,59]	5.208
d_0	1.8-2.2 Å [12]	2.0 Å
B	90-105 meV [1,63]	100 meV
C/B	4.81 [59]	4.81
ζ	2-40 meV [69,70]	15 meV
k	10-20 eV/Å^2 [10]	15 eV/Å^2
κ	0.75-5.5 eV/Å^2 [71]	0.75 eV/Å^2
δ_A	0.08-0.15 Å [12]	0.11 Å
δ_T	0.05-0.10 Å [72,73]	0.05 Å
$Q_T^{(0)}$	0.15-0.20 Å [72,73]	0.15 Å
ω_{HS}	100-500 cm^{-1} [71]	220 cm^{-1}
ω_{LS}	100-500 cm^{-1} [71]	300 cm^{-1}
$\Delta T/\Delta t$	0.3-12.0 K/min	0.3 K/min

The ratio of ligand and metal masses, M/M_0, is trivial to calculate for a given material. Even for SCO complexes with relatively small ligands, like $[\mathrm{Fe(ptz)_6}](\mathrm{BF_4})_2$,[68] $M/M_0 = 1.92$.

δ_T has a large effect on the difference of the angular distortion in LS and HS states, $\Delta\Sigma = \Sigma_{HS} - \Sigma_{LS}$, but only a small influence on average metal-ligand bond length difference, $\Delta d = d_{HS} - d_{LS}$, figure 11. Therefore, we base the value of δ_T on experimental measurements of $\Delta\Sigma$.[72,73]

$Q_T^{(0)}$ strongly affects the average angular distortion of HS and LS states, $\overline{\Sigma} = (\Sigma_{HS} + \Sigma_{LS})/2$, but only has a small influence on the average metal-ligand bond length, $\overline{d} = (d_{HS} + d_{LS})/2$; figure 12. Therefore, the value of this parameter is estimated from experimental measurements of the average angular distortion of the LS state and HS state.[72,73]

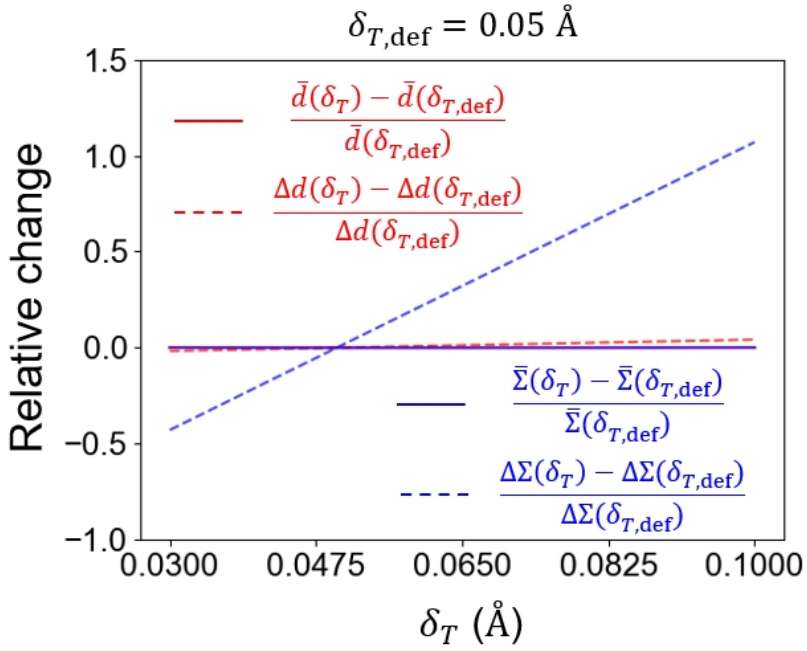

Figure 11: The relationships between the model parameter δ_T and the relative changes of: the average metal-ligand bond length, $\overline{d} = \frac{1}{2}(d_{HS} + d_{LS})$ (red line); the average metal-ligand bond length difference, $\Delta d = d_{HS} - d_{LS}$ (red dashed line); the average angular distortion, $\overline{\Sigma} = \frac{1}{2}(\Sigma_{HS} + \Sigma_{LS})$ (blue line); and the angular distortion difference between the LS and HS states, $\Delta\Sigma = \Sigma_{HS} - \Sigma_{LS}$ (blue dashed line). Here $\delta_{T,\mathrm{def}} = 0.05$ Å is the default value of δ_T (see Table 1); all other model parameters are set to the default values, given in Table 1. Clearly, $\overline{d}$ depends much more strongly on δ_T than $\overline{d}$, Δd, or $\overline{\Sigma}$.

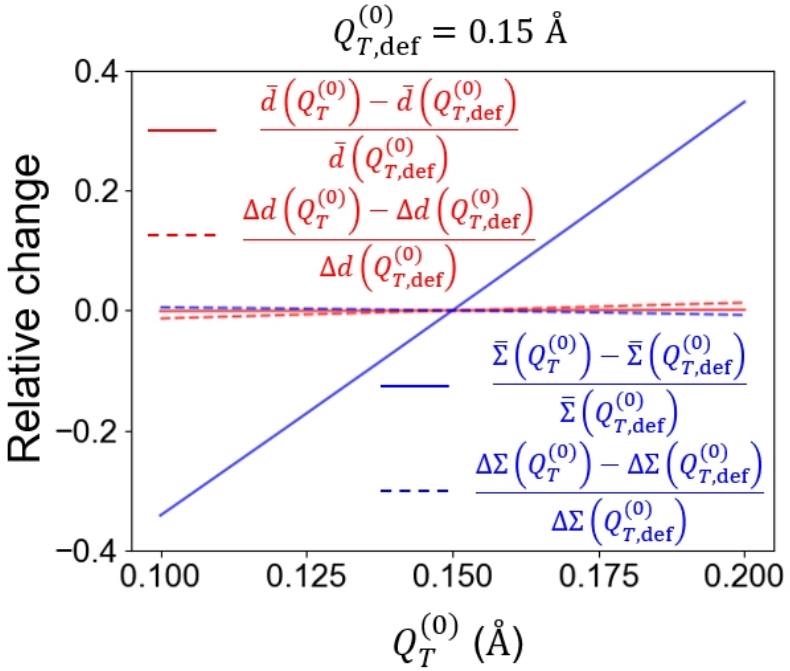

Figure 12: The relationships between the model parameter $Q_T^{(0)}$ and the relative changes of: the average metal-ligand bond length, $\overline{d} = \frac{1}{2}(d_{HS} + d_{LS})$ (red line); the average metal-ligand bond length difference, $\Delta d = d_{HS} - d_{LS}$ (red dashed line); the average angular distortion, $\overline{\Sigma} = \frac{1}{2}(\Sigma_{HS} + \Sigma_{LS})$ (blue line); and the angular distortion difference between the LS and HS states, $\Delta\Sigma = \Sigma_{HS} - \Sigma_{LS}$ (blue dashed line). Here $Q_T^{(0)} = 0.15$ Å is the default value of $Q_T^{(0)}$ (see Table 1); all other model parameters are set to the default values, given in Table 1. Clearly, $\overline{d}$ depends much more strongly on $Q_T^{(0)}$ than $\overline{d}$, Δd, or $\overline{\Sigma}$.

Thermal spin crossover and relaxation following LIESST

The model introduced above provides an explicit construction of a two-dimensional double-well free energy surface in the space of the coordinates Q_A and Q_T that describes the spin crossover between the LS and HS states. To give a detailed description of SCO we use transition state theory (TST)[60] to calculate the transition rates and determine the characteristic temperature of the thermal-induced crossover ($T_{1/2}$), and the highest temperature (T_{LIESST}) for which the trapped state is stable following light-induced spin-state trapping (LIESST).

It is helpful to utilize mass-weighted coordinates,

$$\overline{Q}_A = \sqrt{M_A} Q_A, \tag{18}$$

$$\overline{Q}_T = \sqrt{M_T} Q_T, \tag{19}$$

and denote the seam separating HS and LS states by $\overline{Q}_T = \mathcal{S}(\overline{Q}_A)$. This allows us to write the TST spin crossover rates as

$$k_{\mathrm{L}\to\mathrm{H}}(T) = \sqrt{\frac{k_B T}{2\pi}} \frac{\int e^{-V_{\mathrm{DW}}\left(\overline{Q}_A, \mathcal{S}(\overline{Q}_A)\right)/k_B T} d\overline{Q}_A}{\iint_{\mathrm{L}} e^{-V_{\mathrm{DW}}\left(\overline{Q}_A, \overline{Q}_T\right)/k_B T} d\overline{Q}_A d\overline{Q}_T}, \tag{20}$$

$$k_{\mathrm{H}\to\mathrm{L}}(T) = \sqrt{\frac{k_B T}{2\pi}} \frac{\int e^{-V_{\mathrm{DW}}\left(\overline{Q}_A, \mathcal{S}(\overline{Q}_A)\right)/k_B T} d\overline{Q}_A}{\iint_{\mathrm{H}} e^{-V_{\mathrm{DW}}\left(\overline{Q}_A, \overline{Q}_T\right)/k_B T} d\overline{Q}_A d\overline{Q}_T}, \tag{21}$$

where $\iint_{\mathrm{L}}$ is the integral over the LS area (left of $\mathcal{S}$ in figure 8), $\iint_{\mathrm{H}}$ is the integral over the HS area (right of $\mathcal{S}$ in figure 8). We determine $\mathcal{S}$ from direct inspection of the ground state wavefunctions and perform these integrals numerically via the trapezoidal rule. As the integrated function decays exponentially for $\overline{Q}_T$ far from $\mathcal{S}(\overline{Q}_A)$, we can cut the integral off far from $\mathcal{S}(\overline{Q}_A)$. We set the limits of integration to be -1.0 Å $\leq Q_A \leq 1.0$ Å and $0 \leq Q_T \leq 1.0$ Å. The value of integrand is essentially zero and beyond these limits, figure S3.

Both rates are strongly temperature dependent. At low temperatures, $k_{\mathrm{L}\to\mathrm{H}}$ is less than

$k_{\mathrm{H}\to\mathrm{L}}$, figure 13. This corresponds to a lower free energy of the LS local minimum than in the HS local minimum of the DW free energy surface, and thus a larger barrier for going from LS to HS than the reverse process, figure 10. Thus, in equilibrium, there will be more LS molecules. At high temperatures, $k_{\mathrm{L}\to\mathrm{H}} > k_{\mathrm{H}\to\mathrm{L}}$, as the LS local minimum has higher free energy than the HS local minimum, figure 10. Thus, in equilibrium, there will be more HS molecules. When $k_{\mathrm{L}\to\mathrm{H}} = k_{\mathrm{H}\to\mathrm{L}}$ there will be equal numbers of HS and LS molecules in equilibrium. The temperature at which this occurs defines the characteristic temperature of thermal spin crossover, $T_{1/2}$. This occurs when the barriers for HS→LS and LS→HS are equal. As the transition state is common to both process this implies that the free energies of the two local minima must be equal. Thus, the dynamics reproduce the expected thermodynamic result.

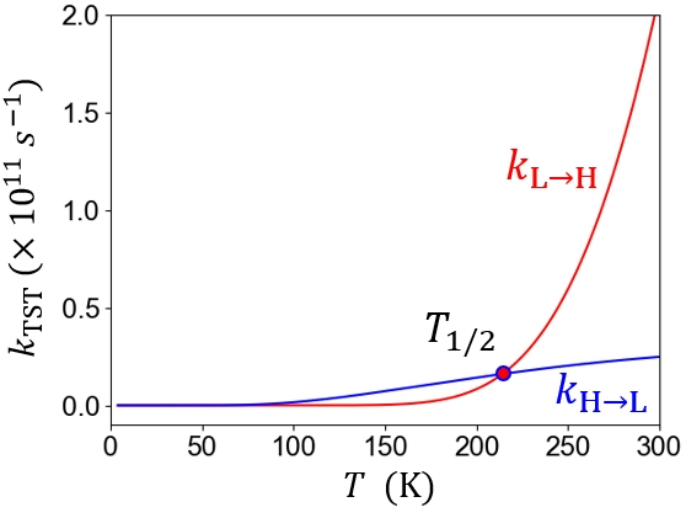

Figure 13: Variation of the transition rates with temperature. At low temperatures, the LS to HS rate ($k_{\mathrm{L}\to\mathrm{H}}$) is lower than the HS to LS rate ($k_{\mathrm{H}\to\mathrm{L}}$), thus in equilibrium there are more LS molecules. At high temperatures $k_{\mathrm{L}\to\mathrm{H}} > k_{\mathrm{H}\to\mathrm{L}}$); thus in equilibrium there are more HS molecules. These two rates are equal at the temperature $T_{1/2}$, whence there are equal numbers of HS and LS molecules in equilibrium. This plot uses the default values of the parameters listed in Table 1.

The chemical rate equations[60] for the HS and LS states are

$$\frac{d\gamma_L(t,T)}{dt} = -k_{\mathrm{L}\to\mathrm{H}}(T)\gamma_L(t,T) + k_{\mathrm{H}\to\mathrm{L}}(T)\gamma_H(t,T), \tag{22a}$$

$$\frac{d\gamma_H(t,T)}{dt} = -k_{\mathrm{H}\to\mathrm{L}}(T)\gamma_H(t,T) + k_{\mathrm{L}\to\mathrm{H}}(T)\gamma_L(t,T), \tag{22b}$$

where γ_{LS} and γ_{HS} are the fractions of LS and HS molecules respectively. As $\gamma_H(t,T) + \gamma_L(t,T) = 1$ for all t and T these have solutions

$$\gamma_L(t,T) = [\gamma_L(0,T) - \gamma_L(\infty,T)]\, e^{-k^*(T)t} + \gamma_L(\infty,T), \tag{23a}$$

$$\gamma_H(t,T) = [\gamma_H(0,T) - \gamma_H(\infty,T)]\, e^{-k^*(T)t} + \gamma_H(\infty,T), \tag{23b}$$

where $k^*(T) = k_{\mathrm{L}\to\mathrm{H}}(T) + k_{\mathrm{H}\to\mathrm{L}}(T)$ is the rate at which the system equilibrates, $\gamma_L(\infty,T) = k_{\mathrm{H}\to\mathrm{L}}(T)/k^*(T)$ is the equilibrium LS fraction, and $\gamma_H(\infty,T) = k_{\mathrm{L}\to\mathrm{H}}(T)/k^*(T)$ is the equilibrium HS fraction.

To simulate cooling from high temperatures, we initialize the system in the all-HS state $[\gamma_H(0,T) = 1;\, \gamma_L(0,T) = 0]$ and then equilibrate at 500 K before lowering the temperature from 500 K to 10 K in steps of ΔT. At each temperature step, we set the initial condition of the system as the final condition of the system at the last temperature step and then let the system evolve according to the rate equations (23) for a time Δt. Thus, the cooling rate is $\Delta T/\Delta t$. After reaching 10 K we then heat the system at the same rate until it returns to 500 K.

We define $T_{1/2,\downarrow}$ ($T_{1/2,\uparrow}$) as the temperature on cooling (resp. heating) when, after the final time step, $\gamma_{LS} = \gamma_{HS} = 1/2$; $T_{1/2} = (T_{1/2,\downarrow} + T_{1/2,\uparrow})/2$; and the hysteresis width as $\Delta T_{1/2} = T_{1/2,\uparrow} - T_{1/2,\downarrow}$. The calculated effect of thermal cycling is shown in figure 14 for two different cooling rates, in the range typically explored experimentally. We do not observe hysteresis, even for unphysically fast cooling/heating rates. From the perspective of equilibrium thermodynamics this is as expected: we are considering a single molecule theory and so

have a crossover and not a first order phase transition. However, in many SCO materials the width of the apparent hysteresis is found to depend strongly on the cooling/heating rate,[74] suggesting that there is a significant contribution from kinetic trapping to the difference in $T_{1/2}$ on cooling and heating. This is entirely absent from our calculations on the timescales relevant to such experiments; suggesting that the relevant kinetic traps are caused by interactions between molecules in the solid state rather than the activation energy required to cross the HS↔LS barrier in a single molecule.

Furthermore, we find that $T_{1/2}$ is independent of the cooling/heating rate, figure 15. This is consistent with recent experiments[75] that show that while heating (cooling) rates can increase (decrease) $T_{1/2,\uparrow}$ (resp. $T_{1/2,\downarrow}$), the average $T_{1/2}$, does not change.

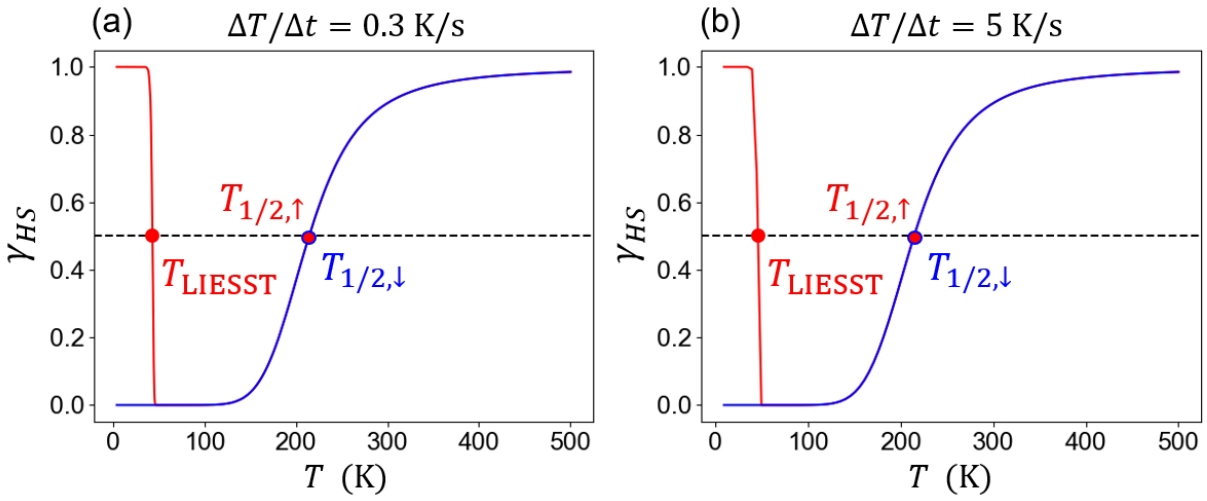

Figure 14: Variation of HS fraction (γ_{HS}) with temperature (T). Both heating (red) and cooling (blue) are initiated in an all HS state. Thus the heating curves model relaxation following, e.g., a LIESST experiment. The heating/cooling rates are (a) $\Delta T/\Delta t = 0.3$ K/s. (b) $\Delta T/\Delta t = 5$ K/s. In both plots, we set $\delta_A = 0.15$ Å. The other parameters are the default values given in Table 1.

To simulate thermal relaxation following LIESST, we initialize the system in the all-HS state and equilibrate at 10 K before raising the temperature from 10 K to 500 K in steps of ΔT. We take T_{LIESST} as the lowest temperature when $\gamma_{HS} = 1/2$ in this simulation. Again we show the results of these simulations for two different heating/cooling rates in figure 14. We find that T_{LIESST} depends strongly on the heating rate, figure 15, in marked contrast to

$T_{1/2}$ and in agreement with experiment.[76]

These results underline that E_b, the height of the barrier in the DW potential, controls T_{LIESST}, as this measures the stability of a metastable state; whereas $T_{1/2}$ is independent of the barrier height as this temperature is determined by thermodynamics, specifically $T_{1/2}$ is the temperature where the free energies of the HS and LS states are equal and hence $k_{H\to L} = k_{L\to H}$. That is, the kinetics are determined by the thermodynamics at $T = T_{1/2}$.

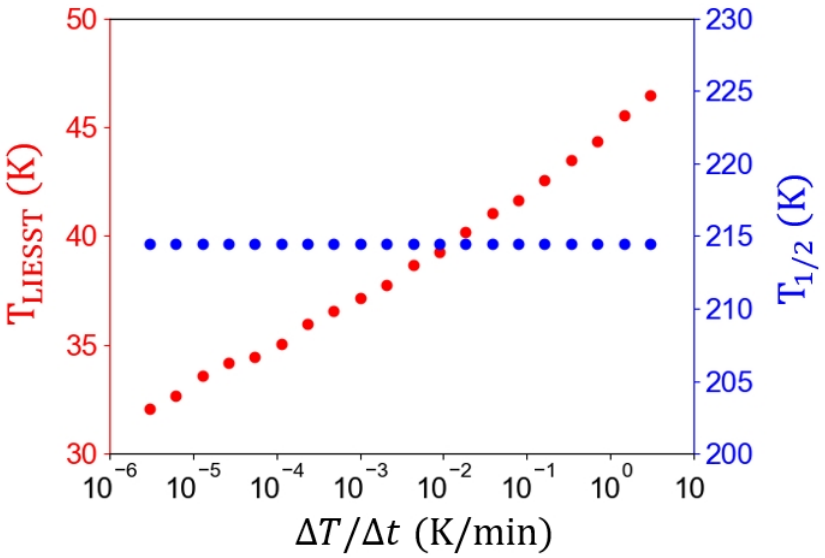

Figure 15: T_{LIESST} (red) depends strongly on the heating rate, $\Delta T/\Delta t$, whereas $T_{1/2}$ (blue) is independent of the heating or cooling rate. Here we set $\delta_A = 0.15$ Å and the other parameters are the default values, shown in Table 1.

Different SCO complexes will be described by different parameters of the model. Therefore, understanding how different parameters change the macroscopic behaviors (e.g., $T_{1/2}$ and T_{LIESST}) is an important step towards optimizing these behaviors in new materials.

It has been argued[17,77,78] that the stiffness of the inner coordination sphere, k, is a key parameter controlling T_{LIESST}. We find that this still holds true once molecular distortions are included, with stiffer inner coordination spheres (larger k) leading to higher T_{LIESST}, but that the stiffness of the inner coordination sphere has little effect of $T_{1/2}$ in this model, figure 16.

While, they have a simple interpretation within the theory, it is not immediately obvious

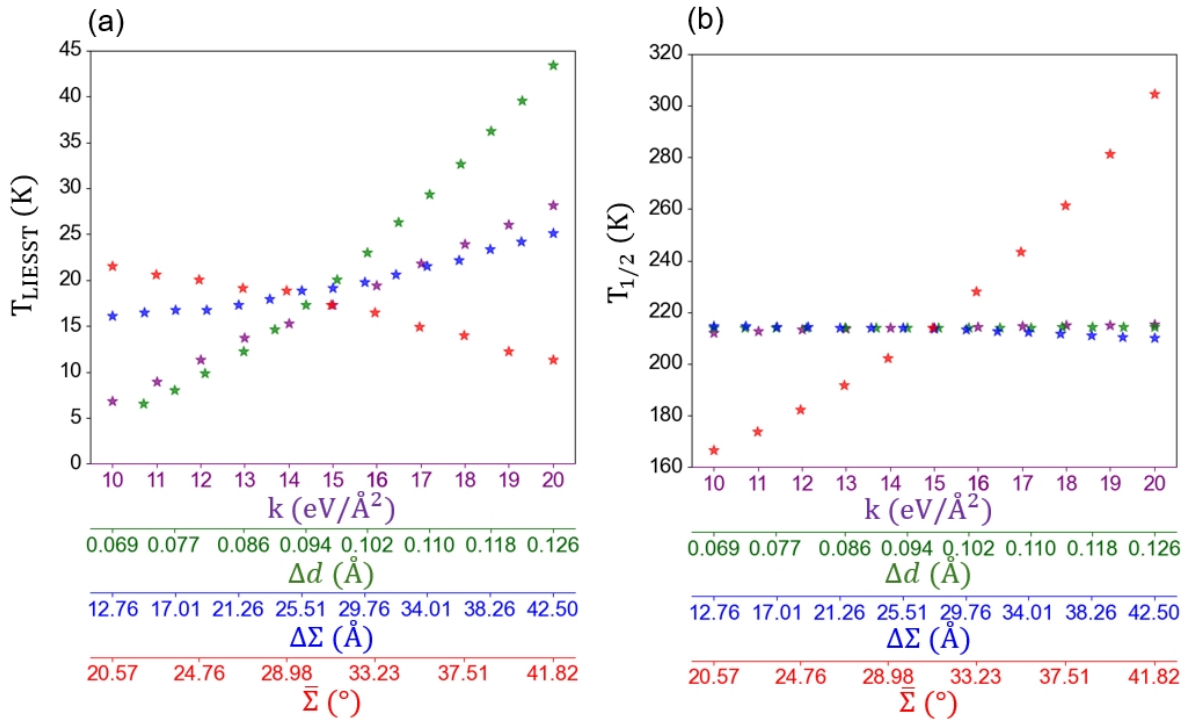

Figure 16: Molecular distortions have (a) a major influence on T_{LIESST} but (b) a minor influence on $T_{1/2}$. Here we show the effect of varying the key microscopic parameters on the (a) T_{LIESST} and (b) $T_{1/2}$. The color of the data points matches the label on the corresponding x-axis. Variations in any of the four parameters causes a similar magnitude of variation in T_{LIESST}, as this is highly sensitive to $k_{H\to L}$. However, only the average angular distortion, $\overline{\Sigma}$, has a significant impact on $T_{1/2}$; as this is the only structural parameter that has a significant impact on ΔH, see figure 9. In these plots the changes in $\Delta d = d_{HS} - d_{LS}$, $\Delta\Sigma = \Sigma_{HS} - \Sigma_{LS}$, and $\overline{\Sigma} = (\Sigma_{HS} + \Sigma_{LS})/2$ are controlled by varying δ_A, δ_T, and $Q_T^{(0)}$ respectively with all other parameters other than the one varied set to their default values, cf. figures 11, 12, and S2. An equivalent plot, figure S4, in terms of the model parameters is reported in the supporting information.

how δ_A, δ_T, and $Q_T^{(0)}$ should be understood in an experimental context. To aid comparison with experiment we calculate the change in the average metal-ligand bond length between the HS and LS states, $\Delta d = d_{HS} - d_{LS}$, as a function of δ_A; the change in angular distortion, $\Delta\Sigma = \Sigma_{HS} - \Sigma_{LS}$, as a function of δ_T; and the average angular distortion, $\overline{\Sigma} = (\Sigma_H + \Sigma_L)/2$, as a function of $Q_T^{(0)}$. In each case all other parameters are set to their default values. This is helpful because changes in Δd, $\Delta\Sigma$, and $\overline{\Sigma}$ are largely driven by δ_A, δ_T, and $Q_T^{(0)}$ respectively, cf. Fig. 11, 12, and S2.

The average metal-ligand bond length difference between HS and LS states (Δd) and the angular distortion difference ($\Delta\Sigma$) have a significant effect of T_{LIESST}, with larger Δd or $\Delta\Sigma$ increasing T_{LIESST}. For reasonable changes in k, Δd and $\Delta\Sigma$ the impact on T_{LIESST} is of a similar magnitude, figure 16. These changes can be understood as increasing k, Δd or $\Delta\Sigma$ increases the barrier between the HS and LS states. This reduces $k_{\mathrm{H}\to\mathrm{L}}$ and hence increases T_{LIESST}, which is determined by dynamics.

However, neither k, Δd nor $\Delta\Sigma$ has a significant effect on $T_{1/2}$, as these three parameters have little influence on the energy difference between the LS and HS local minima, ΔH. This emphasizes that $T_{1/2}$ is a thermodynamic property [as $\Delta t \gg 1/k_{\mathrm{H}\to\mathrm{L}}(T = T_{1/2}) = 1/k_{\mathrm{L}\to\mathrm{H}}(T = T_{1/2})$]. So changes in the barrier height do not affect $T_{1/2}$.

However, $\overline{\Sigma}$ has significant effects on both T_{LIESST} and $T_{1/2}$. As $\overline{\Sigma}$ increases, T_{LIESST} decreases. This is because increasing $\overline{\Sigma}$ increases the energy of the HS local minimum, thus slightly decreasing the potential barrier ΔE_b, see figure 9. This makes it easier to transit from the HS state to the LS state. Furthermore, the average angular distortion has a huge influence on $T_{1/2}$ because variation in $Q_T^{(0)}$ can cause large (e.g., factor of two) changes in ΔH, see 9, with larger $\overline{\Sigma}$ stabilizing the LS state over the HS state (increasing ΔH).

Conclusion

We have introduced a simple model of molecular distortions in SCO complexes, based on crystal field theory. We used this model, and transition state theory, to parameterize chemical rate equations for isolated complexes (i.e., neglecting elastic interactions that occur in the solid state). This allowed us to model the effect of molecular distortions on the key macroscopic temperature scales used to classify SCO complexes: $T_{1/2}$, the characteristic temperature scale parameterizing the thermal crossover; and T_{LIESST}, the maximum temperature at which trapped excited HS states are stable.

We found that the rigidity of the inner coordination sphere (k), the change in the metal-ligand bond length between the HS and LS species ($\Delta d = d_{HS} - d_{LS}$), and the change in the molecular distortion between the HS and LS states ($\Delta\Sigma = \Sigma_{HS} - \Sigma_{LS}$), have very little effect on $T_{1/2}$. However, the average distortion across HS and LS species ($\overline{\Sigma} = (\Sigma_{HS} + \Sigma_{LS})/2$) has a large effect of $T_{1/2}$.

Our model provides a simple explanation of this: $T_{1/2}$ is a purely thermodynamic quantity. At $T = T_{1/2}$, by definition, the number of HS and LS complexes are equal. Thus, the rate constants for going from HS-to-LS and LS-to-HS must be equal [$k_{\mathrm{H}\to\mathrm{L}}(T_{1/2}) = k_{\mathrm{L}\to\mathrm{H}}(T_{1/2})$]. This is only possible if the free energies of the HS and LS states are equal [$G_H = G_L$]. Thus, the thermodynamics entirely determine the kinetics and $T_{1/2}$ is a purely thermodynamic quantity (i.e., the height of the barrier between the HS and LS states has no effect of $T_{1/2}$). We find that k, Δd, and $\Delta\Sigma$ have little impact on the relative free energies of the HS and LS states, and therefore little impact on $T_{1/2}$. But $\overline{\Sigma}$ strongly impacts ΔG (figure 9) and hence $T_{1/2}$.

As we have only considered the single molecule theory we do not expect true, thermodynamic hysteresis. However, interestingly, we do not find any apparent hysteresis; even for cooling/heating rates orders in magnitude in excess of those used experimentally. This contrasts with the experimental situation where the apparent hysteresis width does strongly depend on the cooling/heating rate.[74] This suggests that these kinetic effects in the thermal

transition are driven by intermolecular reactions rather than the single molecule behavior.

In marked contrast, the rigidity of the inner coordination sphere, the change in the metal-ligand bond length between HS and LS species, the change in the molecular distortion between the HS and LS states, and the average distortion between HS and LS species all strongly impact T_{LIESST}. Again, our model provides a simple explanation: that T_{LIESST} is a measure of the dynamics of the system, and not a thermodynamic quantity. T_{LIESST} is effectively a comparison of the decay rate of the trapped HS state to the timescale of the experiment (typically, the heating rate). TST tells us that the decay rate of the metastable HS state is largely set by the barrier height, E_b (i.e., the energy difference between the saddle point of the DW potential and the local HS minimum of the DW potential). As E_b is strongly affected by k, Δd, $\Delta\Sigma$, and $\overline{\Sigma}$ (figure 9), each of these quantities strongly impact T_{LIESST}.

This analysis yields insights into designing SCO complexes with tailored properties. Decreasing the average distortion across HS and LS species will increase T_{LIESST} and decrease $T_{1/2}$, which may be an route to high temperature spin-state switching.[17] Increasing the rigidity of the inner coordination sphere, the change in the metal-ligand bond length between the HS and LS species, and the change in the molecular distortion between the HS and LS states will increase T_{LIESST} without substantially changing $T_{1/2}$.

It has been suggested that increasing T_{LIESST} above $T_{1/2}$ could provide new routes to switching at or above room temperature in 'hidden SCO' materials.[17] Our work provides a specific recipe of how to achieve this.

Acknowledgement

This work was supported by the Australian Research Council (DP230100139).

Supporting Information Available

The following files are available free of charge.

- SupportingInformation.pdf: In this file, we provided additional data detailing the nature of the first excited state, how key structural observables vary with the model parameter δ_A, the error is evaluating the integral in equation 21, and how T_{LIESST} and $T_{1/2}$ vary with key model parameters. We also provide the detailed calculations of the single electron energy terms, d^6 electron-electron interactions, and spin-orbital coupling under C_{4v} symmetric ligand field based on crystal field theory, including tabulation of the relevant wavefunctions.

References

(1) Gütlich, P.; Goodwin, H. Spin Crossover in Transition Metal Compounds I; Spin Crossover in Transition Metal Compounds; Springer, 2004.

(2) Gütlich, P.; Gaspar, A. B.; Garcia, Y. Spin state switching in iron coordination compounds. Beilstein Journal of Organic Chemistry **2013**, 9, 342–391.

(3) Tailleur, E.; Marchivie, M.; Itié, J.-P.; Rosa, P.; Daro, N.; Guionneau, P. Pressure-Induced Spin-Crossover Features at Variable Temperature Revealed by In Situ Synchrotron Powder X-ray Diffraction. Chemistry – A European Journal **2018**, 24, 14495–14499.

(4) Bonhommeau, S.; Molnár, G.; Goiran, M.; Boukheddaden, K.; Bousseksou, A. Unified dynamical description of pulsed magnetic field and pressure effects on the spin crossover phenomenon. Phys. Rev. B **2006**, 74, 064424.

(5) Tiwari, R. K.; Paul, R.; Rajaraman, G. Investigating the influence of oriented external electric fields on modulating spin-transition temperatures in Fe(ii) SCO complexes: a theoretical perspective. Dalton Trans. **2024**, 53, 14623–14633.

(6) Hayami, S.; Gu, Z.-z.; Shiro, M.; Einaga, Y.; Fujishima, A.; Sato, O. First Observation

of Light-Induced Excited Spin State Trapping for an Iron(III) Complex. Journal of the American Chemical Society **2000**, 122, 7126–7127.

(7) Senthil Kumar, K.; Ruben, M. Emerging trends in spin crossover (SCO) based functional materials and devices. Coordination Chemistry Reviews **2017**, 346, 176–205, SI: 42 iccc, Brest– by invitation.

(8) Molnár, G.; Rat, S.; Salmon, L.; Nicolazzi, W.; Bousseksou, A. Spin Crossover Nanomaterials: From Fundamental Concepts to Devices. Advanced Materials **2018**, 30, 1703862.

(9) Kahn, O.; Martinez, C. J. Spin-Transition Polymers: From Molecular Materials Toward Memory Devices. Science **1998**, 279, 44–48.

(10) D'Avino, G.; Painelli, A.; Boukheddaden, K. Vibronic model for spin crossover complexes. Phys. Rev. B **2011**, 84, 104119.

(11) Nicolazzi, W.; Bousseksou, A. Thermodynamical aspects of the spin crossover phenomenon. Comptes Rendus. Chimie **2018**, 21, 1060–1074.

(12) Collet, E.; Guionneau, P. Structural analysis of spin-crossover materials: From molecules to materials. Comptes Rendus. Chimie **2018**, 21, 1133–1151.

(13) Hauser, A. Intersystem crossing in Fe(II) coordination compounds. Coordination Chemistry Reviews **1991**, 111, 275–290.

(14) Enachescu, C.; Linarès, J.; Varret, F. Comparison of static and light-induced thermal hystereses of a spin-crossover solid, in a mean-field approach†. Journal of Physics: Condensed Matter **2001**, 13, 2481.

(15) Nishino, M.; Boukheddaden, K.; Konishi, Y.; Miyashita, S. Simple Two-Dimensional Model for the Elastic Origin of Cooperativity among Spin States of Spin-Crossover Complexes. Phys. Rev. Lett. **2007**, 98, 247203.

(16) Ordejón, B.; de Graaf, C.; Sousa, C. Light-Induced Excited-State Spin Trapping in Tetrazole-Based Spin Crossover Systems. Journal of the American Chemical Society **2008**, 130, 13961–13968.

(17) Nadeem, M.; Cruddas, J.; Ruzzi, G.; Powell, B. J. Toward High-Temperature Light-Induced Spin-State Trapping in Spin-Crossover Materials: The Interplay of Collective and Molecular Effects. Journal of the American Chemical Society **2022**, 144, 9138–9148, PMID: 35546521.

(18) Natt, N.; Powell, B. J. Complex Relaxation of Trapped Spin-States in Spin Crossover Materials. Chem. Sci. **2024**, Accepted Manuscript, https://doi.org/10.1039/D4SC04225E.

(19) Mi, S.; Molnár, G.; Ridier, K.; Nicolazzi, W.; Bousseksou, A. All-atom molecular dynamics simulation of the [Fe(pyrazine)][Ni(CN)$_4$] spin-crossover complex. I. Thermally induced spin transition in the bulk material. Phys. Rev. B **2024**, 109, 054103.

(20) Paez-Espejo, M.; Sy, M.; Boukheddaden, K. Elastic Frustration Causing Two-Step and Multistep Transitions in Spin-Crossover Solids: Emergence of Complex Antiferroelastic Structures. Journal of the American Chemical Society **2016**, 138, 3202–3210.

(21) Cruddas, J.; Powell, B. J. Spin-State Ice in Elastically Frustrated Spin-Crossover Materials. Journal of the American Chemical Society **2019**, 141, 19790–19799.

(22) Cruddas, J.; Powell, B. J. Structure–property relationships and the mechanisms of multistep transitions in spin crossover materials and frameworks. Inorg. Chem. Front. **2020**, 7, 4424–4437.

(23) Boukheddaden, K.; Nishino, M.; Miyashita, S. Molecular Dynamics and Transfer Integral Investigations of an Elastic Anharmonic Model for Phonon-Induced Spin Crossover. Phys. Rev. Lett. **2008**, 100, 177206.

(24) Miyashita, S.; Konishi, Y.; Nishino, M.; Tokoro, H.; Rikvold, P. A. Realization of the mean-field universality class in spin-crossover materials. Phys. Rev. B **2008**, 77, 014105.

(25) Nishino, M.; Boukheddaden, K.; Miyashita, S. Molecular dynamics study of thermal expansion and compression in spin-crossover solids using a microscopic model of elastic interactions. Phys. Rev. B **2009**, 79, 012409.

(26) Nishino, M.; Enachescu, C.; Miyashita, S.; Boukheddaden, K.; Varret, F. m. c. Intrinsic effects of the boundary condition on switching processes in effective long-range interactions originating from local structural change. Phys. Rev. B **2010**, 82, 020409.

(27) Nishino, M.; Singh, Y.; Boukheddaden, K.; Miyashita, S. Tutorial on elastic interaction models for multistep spin-crossover transitions. Journal of Applied Physics **2021**, 130, 141102.

(28) Chastanet, G.; Desplanches, C.; Baldé, C.; Rosa, P.; Marchivie, M.; Guionneau, P. A critical review of the T(LIESST) temperature in spin crossover materials – What it is and what it is not. Chemistry Squared **2018**, 2.

(29) Rosa, P.; Debay, A.; Capes, L.; Chastanet, G.; Bousseksou, A.; Le Floch, P.; Létard, J.-F. Heat- and Light-Induced Spin Transition of an Iron(II) Polymer Containing the 1,2,4,5-Tetrakis(diphenylphosphanyl)benzene Ligand. European Journal of Inorganic Chemistry **2004**, 2004, 3017–3019.

(30) Gütlich, P. Spin crossover in iron(II)-complexes. Metal Complexes. Berlin, Heidelberg, 1981; pp 83–195.

(31) Matouzenko, G. S.; Jeanneau, E.; Verat, A. Y.; de Gaetano, Y. The Nature of Spin Crossover and Coordination Core Distortion in a Family of Binuclear Iron(II) Complexes with Bipyridyl-Like Bridging Ligands. European Journal of Inorganic Chemistry **2012**, 2012, 969–977.

(32) Kepp, K. P. Theoretical Study of Spin Crossover in 30 Iron Complexes. Inorganic Chemistry **2016**, 55, 2717–2727, PMID: 26913489.

(33) Halcrow, M. A. Structure:function relationships in molecular spin-crossover complexes. Chem. Soc. Rev. **2011**, 40, 4119–4142.

(34) Capel Berdiell, I.; Michaels, E.; Munro, O. Q.; Halcrow, M. A. A Survey of the Angular Distortion Landscape in the Coordination Geometries of High-Spin Iron(II) 2,6-Bis(pyrazolyl)pyridine Complexes. Inorganic Chemistry **2024**, 63, 2732–2744, PMID: 38258555.

(35) Halcrow, M. A. Iron(II) complexes of 2,6-di(pyrazol-1-yl)pyridines—A versatile system for spin-crossover research. Coordination Chemistry Reviews **2009**, 253, 2493–2514.

(36) Attwood, M.; Turner, S. S. Back to back 2,6-bis(pyrazol-1-yl)pyridine and 2,2':6',2"-terpyridine ligands: Untapped potential for spin crossover research and beyond. Coordination Chemistry Reviews **2017**, 353, 247–277.

(37) Olguín, J.; Brooker, S. Spin crossover active iron(II) complexes of selected pyrazole-pyridine/pyrazine ligands. Coordination Chemistry Reviews **2011**, 255, 203–240.

(38) Halcrow, M. A. Recent advances in the synthesis and applications of 2,6-dipyrazolylpyridine derivatives and their complexes. New J. Chem. **2014**, 38, 1868–1882.

(39) García-López, V.; Orts-Mula, F.; Palacios-Corella, M.; Clemente-Juan, J.; Clemente-León, M.; Coronado, E. Field-induced slow relaxation of magnetization in a mononuclear Co(II) complex of 2,6-bis(pyrazol-1-yl)pyridine functionalized with a carboxylic acid. Polyhedron **2018**, 150, 54–60.

(40) Rigamonti, L.; Bridonneau, N.; Poneti, G.; Tesi, L.; Sorace, L.; Pinkowicz, D.; Jover, J.; Ruiz, E.; Sessoli, R.; Cornia, A. A Pseudo-Octahedral Cobalt(II) Complex with Bispyra-

zolylpyridine Ligands Acting as a Zero-Field Single-Molecule Magnet with Easy Axis Anisotropy. Chemistry – A European Journal **2018**, 24, 8857–8868.

(41) Ding, Z.-Y.; Meng, Y.-S.; Xiao, Y.; Zhang, Y.-Q.; Zhu, Y.-Y.; Gao, S. Probing the influence of molecular symmetry on the magnetic anisotropy of octahedral cobalt(ii) complexes. Inorg. Chem. Front. **2017**, 4, 1909–1916.

(42) Kershaw Cook, L. J.; Tuna, F.; Halcrow, M. A. Iron(ii) and cobalt(ii) complexes of tris-azinyl analogues of 2,2':6',2"-terpyridine. Dalton Trans. **2013**, 42, 2254–2265.

(43) Rajan, R.; Rajaram, R.; Nair, B. U.; Ramasami, T.; Mandal, S. K. Synthesis, characterisation and superoxide dismutase activity of a manganese(II) complex. J. Chem. Soc., Dalton Trans. **1996**, 2019–2021.

(44) Stamatatos, T. C.; Luisi, B. S.; Moulton, B.; Christou, G. Employment of 2,6-Diacetylpyridine Dioxime as a New Route to High Nuclearity Metal Clusters: Mn6 and Mn8 Complexes. Inorganic Chemistry **2008**, 47, 1134–1144, PMID: 18173267.

(45) Stupka, G.; Gremaud, L.; Bernardinelli, G.; Williams, A. F. Redox state switching of transition metals by deprotonation of the tridentate ligand 2,6-bis(imidazol-2-yl)pyridine. Dalton Trans. **2004**, 407–412.

(46) Capel Berdiell, I.; Michaels, E.; Munro, O. Q.; Halcrow, M. A. A Survey of the Angular Distortion Landscape in the Coordination Geometries of High-Spin Iron(II) 2,6-Bis(pyrazolyl)pyridine Complexes. Inorganic Chemistry **2024**, 63, 2732–2744, PMID: 38258555.

(47) Wu, H.; Kou, F.; Jia, F.; Liu, B.; Yuan, J.; Bai, Y. A V-shaped ligand 1,3-bis(1-methylbenzimidazol-2-yl)-2-oxapropane and its Cu(II) complex: Synthesis, crystal structure, antioxidation and DNA-binding properties. Journal of Photochemistry and Photobiology B: Biology **2011**, 105, 190–197.

(48) Migita, C. T.; Migita, K.; Iwaizumi, M. Electron paramagnetic resonance studies of highly anisotropic low-spin states of ferrimyoglobin derivatives. Biochimica et Biophysica Acta (BBA) - Protein Structure and Molecular Enzymology **1983**, 743, 290–298.

(49) Dumitru, F.; Legrand, Y.-M.; Van der Lee, A.; Barboiu, M. Constitutional self-sorting of homochiral supramolecular helical single crystals from achiral components. Chem. Commun. **2009**, 2667–2669.

(50) Burrows, K.; Kulmaczewski, R.; Cespedes, O.; Barrett, S.; Halcrow, M. The Speciation of Homochiral and Heterochiral Diastereomers of Homoleptic Cobalt(II) and Zinc(II) PyBox Complexes. Polyhedron **2018**, 149, 134–141, © 2018 Elsevier Ltd. This is an author produced version of a paper published in Polyhedron. Uploaded in accordance with the publisher's self-archiving policy.

(51) Pringouri, K.; Anwar, M. U.; Mansour, L.; Doupnik, N.; Beldjoudi, Y.; Gavey, E. L.; Pilkington, M.; Rawson, J. M. A novel bis-1,2,4-benzothiadiazine pincer ligand: synthesis, characterization and first row transition metal complexes. Dalton Trans. **2018**, 47, 15725–15736.

(52) Pask, C. M.; Greatorex, S.; Kulmaczewski, R.; Baldansuren, A.; McInnes, E. J. L.; Bamiduro, F.; Yamada, M.; Yoshinari, N.; Konno, T.; Halcrow, M. A. Elucidating the Structural Chemistry of a Hysteretic Iron(II) Spin-Crossover Compound From its Copper(II) and Zinc(II) Congeners. Chemistry – A European Journal **2020**, 26, 4833–4841.

(53) Capel Berdiell, I.; Michaels, E.; Munro, O. Q.; Halcrow, M. A. A Survey of the Angular Distortion Landscape in the Coordination Geometries of High-Spin Iron(II) 2,6-Bis(pyrazolyl)pyridine Complexes. Inorganic Chemistry **2024**, 63, 2732–2744, PMID: 38258555.

(54) Sertphon, D.; Harding, D. J.; Harding, P.; Murray, K. S.; Moubaraki, B.; Adams, H.; Alkaş, A.; Telfer, S. G. Substituent-Influenced Spin Crossover in FeIII Quinolylsalicylaldiminates. European Journal of Inorganic Chemistry **2016**, 2016, 432–438.

(55) Takahashi, K.; Sakurai, T.; Zhang, W.-M.; Okubo, S.; Ohta, H.; Yamamoto, T.; Einaga, Y.; Mori, H. Spin-Singlet Transition in the Magnetic Hybrid Compound from a Spin-Crossover Fe(III) Cation and π-Radical Anion. Inorganics **2017**, 5.

(56) Ketkaew, R.; Tantirungrotechai, Y.; Harding, P.; Chastanet, G.; Guionneau, P.; Marchivie, M.; Harding, D. J. OctaDist: a tool for calculating distortion parameters in spin crossover and coordination complexes. Dalton Trans. **2021**, 50, 1086–1096.

(57) Marchivie, M.; Guionneau, P.; Létard, J.-F.; Chasseau, D. Photo-induced spin-transition: the role of the iron(II) environment distortion. Acta Crystallographica Section B **2005**, 61, 25–28.

(58) Boilleau, C.; Suaud, N.; Guihéry, N. Ab initio study of the influence of structural parameters on the potential energy surfaces of spin-crossover Fe(II) model compounds. The Journal of Chemical Physics **2012**, 137, 224304.

(59) Sugano, S.; Tanabe, Y.; Kamimura, H. Multiplets of Transition-Metal Ions in Crystals; Academic Press, 1970.

(60) Nitzan, A. Chemical Dynamics in Condensed Phases: Relaxation, Transfer and Reactions in Conden Oxford University Press, 2006.

(61) Levine, B. G.; Martínez, T. J. Isomerization Through Conical Intersections. Annual Review of Physical Chemistry **2007**, 58, 613–634.

(62) Griffith, J. The Theory of Transition-Metal Ions; Cambridge University Press, 1961.

(63) Buhks, E.; Navon, G.; Bixon, M.; Jortner, J. Spin conversion processes in solutions. Journal of the American Chemical Society **1980**, 102, 2918–2923.

(64) Khosla, A. L.; Jacko, A. C.; Merino, J.; Powell, B. J. Spin-orbit coupling and strong electronic correlations in cyclic molecules. Phys. Rev. B **2017**, 95, 115109.

(65) Powell, B. J.; Kenny, E. P.; Merino, J. Dynamical Reduction of the Dimensionality of Exchange Interactions and the "Spin-Liquid" Phase of κ-(BEDT$-$TTF)$_2X$. Phys. Rev. Lett. **2017**, 119, 087204.

(66) Powell, B. J.; Merino, J.; Khosla, A. L.; Jacko, A. C. Heisenberg and Dzyaloshinskii-Moriya interactions controlled by molecular packing in trinuclear organometallic clusters. Phys. Rev. B **2017**, 95, 094432.

(67) Wajnflasz, J. Etude de la transition "Low Spin"-"High Spin" dans les complexes octaédriques d'ion de transition. physica status solidi (b) **1970**, 40, 537–545.

(68) Lakhloufi, S.; Guionneau, P.; Lemée-Cailleau, M. H.; Rosa, P.; Létard, J.-F. Structural phase transition in the spin-crossover complex $[Fe(ptz)_6](BF_4)_2$ studied by x-ray diffraction. Phys. Rev. B **2010**, 82, 132104.

(69) Dunn, T. M. Spin-orbit coupling in the first and second transition series. Trans. Faraday Soc. **1961**, 57, 1441–1444.

(70) Kondo, M.; Yoshizawa, K. A theoretical study of spin-orbit coupling in an Fe(II) spin-crossover complex. Mechanism of the LIESST effect. Chemical Physics Letters - CHEM PHYS LETT **2003**, 372, 519–523.

(71) Gütlich, P.; Goodwin, H. Spin Crossover in Transition Metal Compounds III; Spin Crossover in Transition Metal Compounds; Springer, 2004.

(72) Carbonera, C.; Sánchez Costa, J.; Money, V. A.; Elhaïk, J.; Howard, J. A. K.; Halcrow, M. A.; Létard, J.-F. Photomagnetic properties of iron(ii) spin crossover com-

plexes of 2,6-dipyrazolylpyridine and 2,6-dipyrazolylpyrazine ligands. Dalton Trans. **2006**, 3058–3066.

(73) Zenno, H.; Sekine, Y.; Zhang, Z.; Hayami, S. Solvation/desolvation induced reversible distortion change and switching between spin crossover and single molecular magnet behaviour in a cobalt(ii) complex. Dalton Trans. **2024**, 53, 5861–5870.

(74) Brooker, S. Spin crossover with thermal hysteresis: practicalities and lessons learnt. Chem. Soc. Rev. **2015**, 44, 2880–2892.

(75) Traiche, R.; Sy, M.; Oubouchou, H.; Bouchez, G.; Varret, F.; Boukheddaden, K. Spatiotemporal Observation and Modeling of Remarkable Temperature Scan Rate Effects on the Thermal Hysteresis in a Spin-Crossover Single Crystal. The Journal of Physical Chemistry C **2017**, 121, 11700–11708.

(76) Paradis, N.; Chastanet, G.; Palamarciuc, T.; Rosa, P.; Varret, F.; Boukheddaden, K.; Létard, J.-F. Detailed Investigation of the Interplay Between the Thermal Decay of the Low Temperature Metastable HS State and the Thermal Hysteresis of Spin-Crossover Solids. The Journal of Physical Chemistry C **2015**, 119, 20039–20050.

(77) Létard, J.-F.; Guionneau, P.; Nguyen, O.; Costa, J. S.; Marcén, S.; Chastanet, G.; Marchivie, M.; Goux-Capes, L. A Guideline to the Design of Molecular-Based Materials with Long-Lived Photomagnetic Lifetimes. Chemistry – A European Journal **2005**, 11, 4582–4589.

(78) Marcén, S.; Lecren, L.; Capes, L.; Goodwin, H.; Létard, J.-F. Critical temperature of the LIESST effect in a series of hydrated and anhydrous complex salts [Fe(bpp)2]X2. Chemical Physics Letters **2002**, 358, 87–95.